*photonics*

MDPI

*Article*

# Ultrasensitive Exhaled Gas Detection via Evanescent Wave-Excited Fiber SERS Sensor Assembled with Silver Nanocubes

**Wei Wang [1,2,3], Yudong Su [1,2,3], Tong Wu [1,2,3], Pan Tao [4], Kai Zheng [1,2,3], Zheng Zhang [1,2,3,*], Jun Zhou [1,2,3], Shixun Dai [1,2,3] and Peiqing Zhang [1,2,3,*]**

1 Laboratory of Infrared Material and Devices, Advanced Technology Research Institute, Ningbo University, Ningbo 315211, China
2 Zhejiang Key Laboratory of Advanced Optical Functional Materials and Devices, Ningbo University, Ningbo 315211, China
3 Engineering Research Center for Advanced Infrared Photoelectric Materials and Devices of Zhejiang Province, Ningbo University, Ningbo 315211, China
4 Department of Optical Engineering, School of Electronic Science and Engineering, Southeast University, Nanjing 211189, China
* Correspondence: zhangzheng@nbu.edu.cn (Z.Z.); zhangpeiqing@nbu.edu.cn (P.Z.)

**Abstract**

Exhaled breath analysis offers a non-invasive route for metabolic monitoring and disease screening, but its practical implementation requires sensing platforms that combine high sensitivity, robustness, and simplicity. Here, we report an evanescent wave-excited fiber-optic surface-enhanced Raman scattering (SERS) sensor based on silver nanocubes (Ag NCs) assembled onto a fiber taper waist (FTW), and the design is further extended to an Ag/graphene oxide (GO) hybrid interface for enhanced gas detection. Finite element and finite-difference time-domain simulations were employed to optimize the FTW geometry and Ag NC dimensions for efficient evanescent-field excitation and plasmonic enhancement. The fabricated FTW-SERS probe achieved a minimum detectable concentration of $10^{-9}$ M for crystal violet, together with good linearity and a relative standard deviation below 5%. For gas sensing, ethanol and acetone vapors were detected down to 50 ppm using the Ag NC-based FTW-SERS probe. After introducing a 0.3 mg/mL GO functional layer, the minimum detectable concentrations of both analytes were further reduced to 25 ppm. In addition, proof-of-concept monitoring of exhaled ethanol after alcohol consumption revealed dynamic spectral changes consistent with ethanol metabolism. These results demonstrate the potential of evanescent wave-excited FTW-SERS probes for compact and sensitive breath-analysis applications.

**Keywords:** SERS; evanescent wave; fiber taper waist; silver nanocubes; exhaled breath analysis

Check for updates

Received: 13 April 2026
Revised: 26 April 2026
Accepted: 29 April 2026
Published: 5 May 2026

**Copyright:** © 2026 by the authors. Licensee MDPI, Basel, Switzerland. This article is an open access article distributed under the terms and conditions of the Creative Commons Attribution (CC BY) license.

## 1. Introduction

Exhaled breath contains various volatile organic compounds (VOCs) and inorganic gases that reflect ongoing metabolic processes in the human body, making it an attractive medium for non-invasive diagnostics [1–3] (as shown in Figure 1). Many studies have demonstrated that specific VOC signatures can serve as biomarkers for respiratory diseases, metabolic disorders, and even cancer [4,5]. While breath analysis enables continuous and real-time monitoring unlike blood or tissue biopsies [6–8], achieving the analytical reliability and sensitivity required for clinical diagnostics remains a significant challenge [7,9,10].

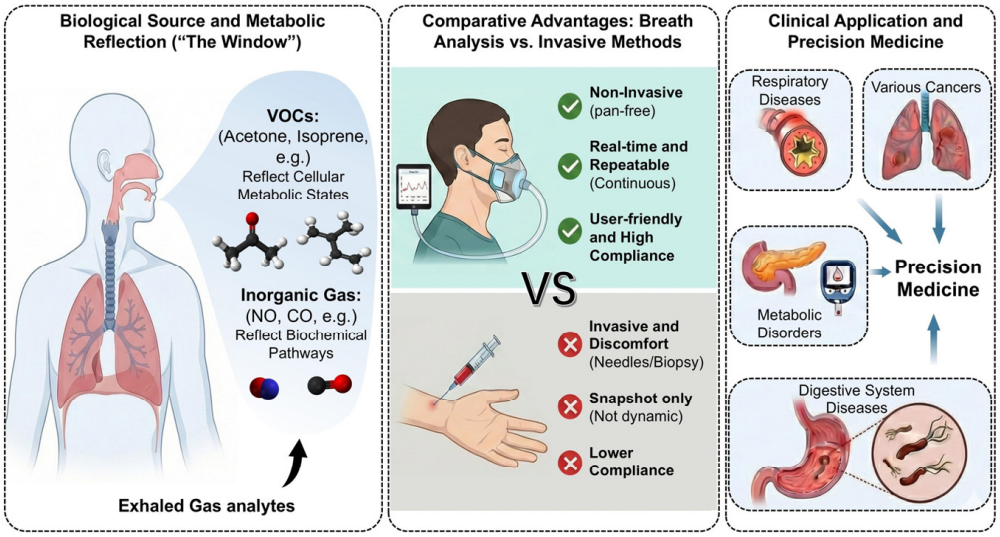



**Figure 1.** Overview of breath analysis for exhaled gas analytes.

Gas chromatography–mass spectrometry (GC-MS) is the current standard for breath analysis due to its high sensitivity and molecular specificity [11,12], but its reliance on bulky instrumentation, complex sample preparation, and offline analysis significantly limits point-of-care use [13,14]. Electronic gas sensors, often referred to as e-noses, provide a more compact alternative, but their performance is frequently compromised by humidity interference, signal drift, and limited selectivity in complex gas mixtures [15,16]. Consequently, there remains a clear gap between laboratory-grade analytical capability and portable, real-time gas sensor systems.

Surface-Enhanced Raman Scattering (SERS) provides a solution by offering molecular-level specificity combined with high sensitivity. Integrating SERS with optical fibers further enables remote sensing and flexible light delivery in confined environments. While configurations like hollow-core photonic crystal fibers can extend the light-analyte interaction length to improve detection performance [17], they typically involve complex fabrication and demanding optical alignment. Conversely, fiber-tip SERS probes are structurally simpler, but often suffer from localized laser heating, which can degrade plasmonic nanostructures and destabilize the sensing signal [18]. Balancing sensitivity, stability, and system complexity is therefore a central challenge in fiber-SERS gas sensor design.

In this work, we present an evanescent wave-excited fiber-optic SERS gas sensor based on a fiber taper waist (FTW) functionalized with silver nanocubes (Ag NCs). By exploiting the evanescent field distributed along the tapered fiber, optical excitation is extended over the entire sensing region rather than being confined to a localized focal spot, thereby enhancing the effective light–matter interaction volume and mitigating localized photothermal effects. The integration of Ag NCs provides strong plasmonic enhancement through the formation of densely distributed electromagnetic hotspots. Furthermore, a graphene oxide (GO) layer is introduced to construct an Ag/GO hybrid interface, which offers additional chemical enhancement via charge-transfer interactions and improves molecular adsorption capability. As a result, the proposed sensor enables sensitive detection of representative volatile organic compounds (VOCs), such as ethanol and acetone, and supports real-time monitoring of exhaled breath. These features highlight the potential of the FTW-based SERS platform as a compact, alignment-free, and highly sensitive solution for practical gas sensing applications.

## 2. Design and Fabrication Experiments

### *2.1. Design Simulation and Optimization of the FTW-SERS Probe*

To optimize the evanescent field intensity within the sensing region, Finite Element Method (FEM) simulations were conducted on the FTW structure [19]. The penetration depth ($d_p$), defined as the distance at which the electric field amplitude decays to 1/e of its value at the interface, is described by Equation (1) [20]:

$$d_p = \frac{\lambda}{2\pi n_1 (\sin^2\theta - \sin^2\theta_c)^{\frac{1}{2}}} \quad (1)$$

where $\lambda$ is the wavelength of the incident light, $n_1$ and $n_2$ are the refractive indices of the core and cladding, respectively, and $\theta$ is the incident angle relative to the normal of the interface. The critical angle $\theta_c$ is defined as [20]:

$$\theta_c = \sin^{-1}(\frac{n_2}{n_1}) \quad (2)$$

Equations (1) and (2) indicate that a reduced FTW diameter shifts the propagation angle $\theta$ toward the critical angle $\theta_c$. This geometric change inherently expands the evanescent field penetration depth. The FEM results in Figure 2 quantitatively verify this trend, showing a pronounced enhancement of the evanescent field intensity as the taper diameter decreases. Unlike the 50 μm FTW, where the optical mode remains largely confined within the fiber core (Figure 2a), the 5 μm FTW exhibits a significantly extended evanescent field at the fiber surface (Figure 2d). This result confirms that tapering effectively promotes field leakage from the guided mode, thereby creating a more favorable excitation configuration for SERS. However, while a smaller diameter enhances the evanescent field, an optimal balance must be struck with practical sensor robustness. Therefore, a diameter of 10 μm was selected for the FTW in subsequent experiments. This choice represents an optimal compromise: a diameter as small as 5 μm, despite its strong field, leads to excessively high optical power density that can thermally damage the assembled Ag NCs and compromise their plasmonic activity, in addition to suffering from poor mechanical rigidity. Conversely, a diameter larger than 10 μm results in a substantially weakened evanescent field, which is insufficient to efficiently excite SERS signals and would limit the ultimate detection sensitivity. The 10 μm FTW thus optimally balances a strong evanescent field for high sensitivity with the necessary mechanical stability and nanostructure integrity for reliable sensing, improving the potential for high-sensitivity detection.

To further optimize the plasmonic substrate, finite-difference time-domain (FDTD) simulations were performed to evaluate the size-dependent electromagnetic response of Ag NC dimers with edge lengths of 35, 45, and 55 nm [21]. In the simulation model, the vertex-to-vertex gap was fixed at 2 nm, and a 785 nm plane wave polarized along the dimer axis (x-axis) was introduced along the negative y-direction [22]. As shown in Figure 2e–g, the local electromagnetic field distribution is strongly dependent on nanocube size. For the 35 nm dimers, the hotspots are highly confined within the narrow junction region (<10 nm), with a maximum field intensity of 15 V/m. In comparison, the 45 nm and 55 nm dimers exhibit substantially enlarged enhancement regions extending along the cube edges, indicating more spatially distributed plasmonic coupling. The 55 nm dimers exhibit optimal plasmonic performance, as they generate a 3.2-fold larger hotspot volume and a broader field distribution. This extended field, driven by multipolar coupling, provides a robust spatial overlap for analyte-field interactions. On this basis, Ag NCs with an edge length of 55 nm were selected for subsequent synthesis and sensor fabrication.

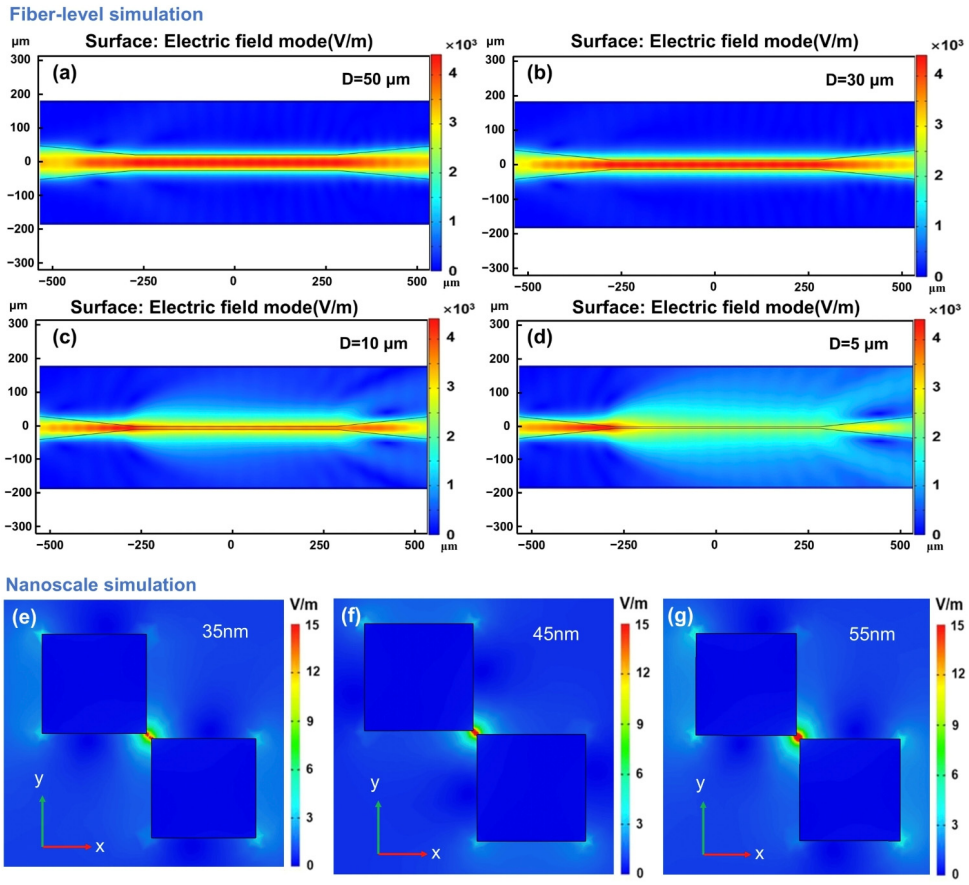



**Figure 2.** Electric field intensity distribution of evanescent waves in FTWs with different diameters: (**a**) 50 μm, (**b**) 30 μm, (**c**) 10 μm, (**d**) 5 μm. Simulated electric field distributions of Ag NCs with a fixed vertex spacing of 2 nm and varying particle sizes: (**e**) 35 nm; (**f**) 45 nm; (**g**) 55 nm.

### *2.2. Fabrication of the FTW-SERS Probe*

Silica FTWs were fabricated using a flame-heating and stepper-motor stretching technique (Figure 3). A stripped quartz fiber was secured on a translation stage (Figure 3a) and heated by a hydrogen-oxygen flame (~3000 °C) to ensure impurity-free processing (Figure 3b). Under computer-controlled uniform stretching (Figure 3c), the fiber was drawn into a tapered structure (Figure 3d). The FTW diameter represents a trade-off between sensitivity and mechanical stability. While smaller diameters enhance evanescent wave leakage, excessive tapering compromises structural rigidity, rendering the fiber susceptible to fracture. Balancing evanescent leakage with structural rigidity, we adopted a 10 μm waist diameter for all fabricated probes (Figure 3d,e).

As shown in Figure 3g, Ag NCs were synthesized by a hydrothermal route using glucose as the reducing agent and cetyltrimethylammonium bromide (CTAB) as the capping agent. The reduction in the silver ammonia complex by glucose is described by Equation (3) [23]:

$$\begin{aligned} &CH_{20}H-(CHOH)_4-CHO+2[Ag(NH_3)_2]^+ + 2OH^- \\ &\rightarrow CH_{20}H-(CHOH)_4-COOH+2Ag+H_2O+2NH_3 \end{aligned} \quad (3)$$

In this process, CTAB acts as a facet-selective structure-directing agent, preferentially adsorbing onto specific crystal planes and thereby suppressing their growth kinetics, which promotes the formation of cubic nanostructures. Based on this mechanism, the silver ammonia precursor was first prepared by adding ammonia dropwise to an aqueous $AgNO_3$ solution (0.17 g) until the initially formed precipitate completely dissolved, followed by

dilution to 20 mL to obtain a 10 mM precursor solution. Subsequently, 5 mL of the precursor was mixed with 5 mL of CTAB solution (75 mM) and 10 mL of glucose solution (1.5 mM). The resulting mixture was transferred into a Teflon-lined autoclave and maintained at 120 °C for 8 h. After the reaction, the Ag NCs were collected by centrifugation at 6000 rpm for 20 min and washed three times with deionized water to remove residual reactants and improve product purity [24].

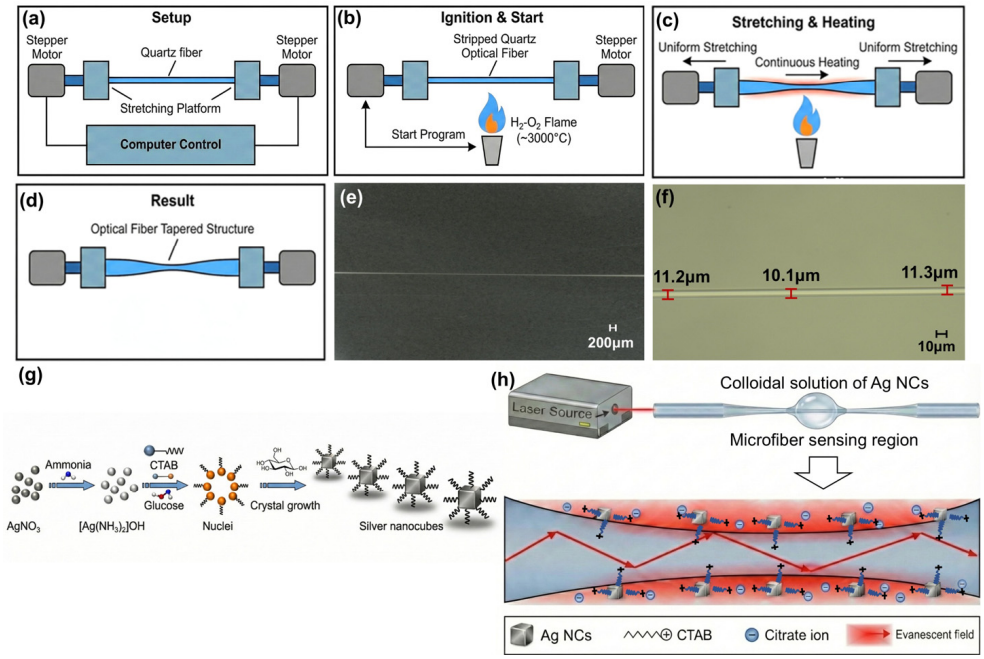



**Figure 3.** Schematic illustration of the FTW fabrication process: (**a**) parameter configuration via the computer control system; (**b**) heating of the optical fiber using a hydrogen-oxygen flame; (**c**) stretching motion driven by stepper motors; (**d**) the fabricated fiber taper waist (FTW); (**e**) overview image of FTW; (**f**) microscopic image of FTW at 500× magnification; (**g**) preparation process of Ag NCs; (**h**) schematic diagram of the FTW SERS probe.

The Ag NC-functionalized FTW probe was fabricated using an evanescent-wave-assisted electrostatic assembly strategy, as illustrated in Figure 3h. Before deposition, the FTW was fixed onto a glass substrate with UV-curable adhesive to ensure mechanical stability during the assembly process. To improve the electrostatic interaction between the silica surface and the positively charged Ag NCs, the FTW was immersed in sodium citrate solution for 1 h to tailor its surface charge properties. The pretreated fiber was then rinsed thoroughly with deionized water and dried in air.

For nanoparticle assembly, a 785 nm continuous-wave laser was coupled into the fiber core through a microscope objective. According to the optimization results in Section 3.2, the excitation power was set to 90 mW to generate a stable evanescent field at the taper waist. For nanoparticle assembly, we applied a Ag NC colloidal droplet to the sensing region. The 90 mW guided laser generates an evanescent optical gradient force, which overcomes Brownian motion to physically trap the nanoparticles onto the silica surface. The deposition process was maintained until complete solvent evaporation, which required approximately 20 min. Finally, the assembled probe was rinsed with deionized water to remove weakly adsorbed nanoparticles and dried under ambient conditions, yielding a robust FTW-SERS sensor with a uniform and high-density Ag NC distribution on the taper surface.

### 2.3. Characterization and Measurement

SERS signal acquisition was performed using a custom-built portable Raman detection platform designed for high-sensitivity interfacial sensing, as depicted in Figure 4a. A 785 nm frequency-stabilized multimode laser served as the excitation source, which was coupled into the proximal end of the Raman probe and precisely focused onto the fabricated FTW-SERS sensor via a microscope objective. The sensing mechanism leverages the unique waveguiding properties of the fiber taper: as the excitation light propagates within the fiber core via total internal reflection, the evanescent field significantly penetrates the cladding at the tapered waist. This evanescent field interacts with the synthesized Ag NCs decorated on the fiber surface, inducing localized surface plasmon resonance (LSPR). This interaction generates dense electromagnetic "hotspots" that amplify the Raman scattering of the adsorbed molecules. The resulting SERS signals are collected through the same optical fiber, back-propagated to the probe module, and directed into a portable spectrometer for spectral analysis.

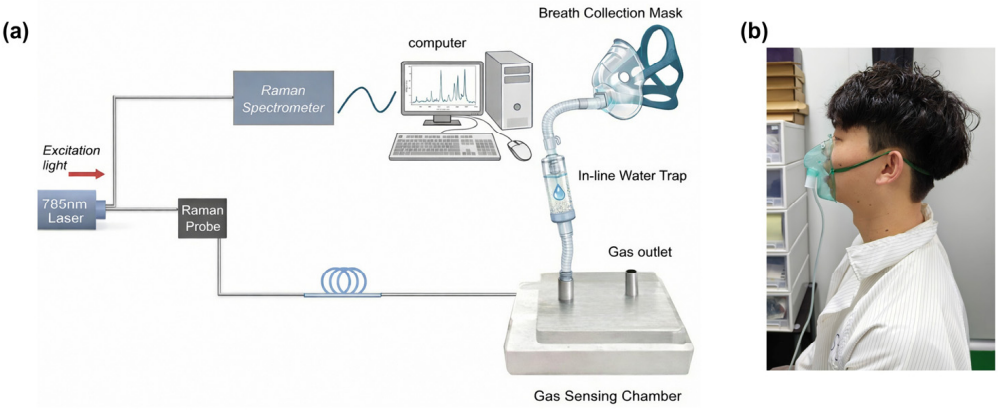



**Figure 4.** (**a**) Schematic diagram of the gas detection setup integrating the FTW-SERS probe. (**b**) Photograph of a participant wearing the breath collection mask.

To facilitate controlled gas-phase measurements under constant temperature and humidity conditions, the FTW-SERS sensor was hermetically sealed within a customized pressurized gas chamber equipped with precision inlet and outlet ports to maintain pressure equilibrium. Spectral data were acquired using an integration time of 1 s. Initially, pure nitrogen ($N_2$) was introduced into the chamber to record the spectral background. All raw spectra subsequently underwent background correction by subtracting the intrinsic Raman signature of the silica fiber to isolate analyte-specific signals. Following this, mass flow controllers were utilized to precisely regulate the mixing ratio of the target gas and nitrogen, enabling the detection of the analyte at various concentrations. For exhaled breath collection, a water vapor removal module was integrated into the facemask device to minimize the influence of moisture on the SERS detection.

The analytical performance of the sensor was validated through a three-phase experimental protocol. First, the baseline SERS activity was quantitatively evaluated using crystal violet (CV) as a standard reporter molecule. Second, the sensor's responsiveness to VOCs was assessed under laboratory conditions using standard ethanol and acetone vapors at concentrations ranging from 25 ppm to 200 ppm. Finally, its clinical utility was demonstrated via an in vivo pharmacokinetic study—as illustrated in Figure 4b—wherein exhaled breath samples from a healthy volunteer were collected and analyzed at 30, 60, 90, and 180 min following the consumption of 500 mL of beer (5% $v/v$ alcohol).

## 3. Results and Discussion

### *3.1. Characterization of Ag NCs and Their Assembly on the FTW Surface*

The morphology of the synthesized Ag NCs was characterized by scanning electron microscopy (SEM). As shown in Figure 5a, the nanoparticles exhibit a uniform cubic morphology with an average edge length of approximately 55 nm, in good agreement with the simulation-guided design. This consistency is critical for generating a homogeneous plasmonic response across the substrate.

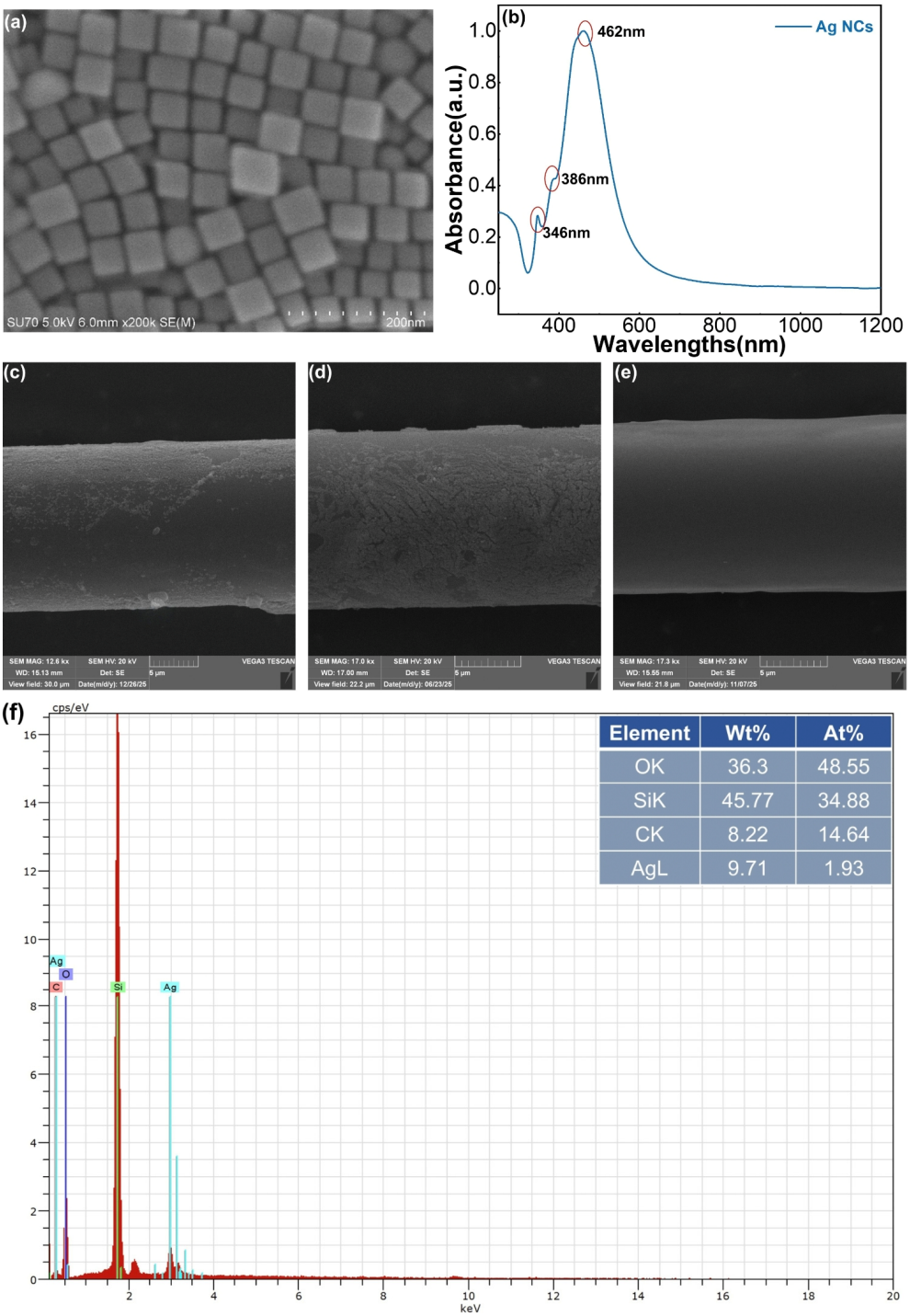



**Figure 5.** (**a**) SEM image of silver nanocubes; (**b**) UV–visible absorption spectrum of silver nanocubes. Deposition of Ag NCs on the FTW surface induced at different laser powers: (**c**) 70 mW, (**d**) 90 mW, and (**e**) 110 mW. (**f**) Energy-dispersive X-ray (EDX) spectrum and elemental composition analysis at the marked point on the fiber taper waist.

The optical properties of the Ag NCs were further examined by UV–Vis absorption spectroscopy (Figure 5b). Three distinct extinction peaks located at 346, 386, and 462 nm were observed, which are characteristic of Ag NCs and can be assigned to their multipolar and dipolar surface plasmon resonance (SPR) modes. The sharp corners of these nanocubes drive a strong lightning-rod effect, producing the high-density electromagnetic hotspots required for localized SERS.

The deposition of Ag NCs onto the FTW surface was achieved through a controllable laser-induced evanescent-wave-assisted assembly process. Since laser power directly affects the local field intensity and deposition dynamics, it was selected as the key parameter for optimization. To identify the optimal assembly condition, the deposition behavior was investigated at laser powers of 70, 90, and 110 mW with a fixed deposition time of 20 min. As shown in Figure 5c–e, the morphology of the deposited layer strongly depends on the excitation power. At 70 mW, the evanescent field is too weak to effectively trap and accumulate nanoparticles on the fiber surface, resulting in a sparse and discontinuous distribution (Figure 5c). Increasing the power to 90 mW produces a densely packed, well-dispersed monolayer on the FTW surface (Figure 5d). However, an excitation of 110 mW triggers excessive aggregation and multi-layer stacking due to accelerated solvent evaporation and amplified optical trapping forces (Figure 5e), which obscures the nanocube edges and degrades surface uniformity. Energy-dispersive X-ray spectroscopy (EDX) of the 90 mW-deposited layer (Figure 5f) confirms the presence of Ag alongside the silica-derived Si and O signals. Consequently, 90 mW was adopted as the standard assembly power.

### *3.2. Analytical Performance Evaluation of the SERS Probe*

The analytical performance of the fabricated FTW-SERS probe was evaluated using crystal violet (CV) as a model analyte. Two characteristic Raman bands at 1177 and 1623 $cm^{-1}$, assigned to in-plane C-H bending and aromatic C-C stretching vibrations, respectively, were selected for quantitative analysis [25]. SERS spectra were collected from CV solutions with concentrations ranging from $10^{-9}$ to $10^{-5}$ M using the optimized probe. For each concentration, measurements were repeated three times, and the average spectrum was used for subsequent analysis. As shown in Figure 6a, the characteristic Raman features remain clearly distinguishable even at $10^{-6}$ M, indicating the high sensitivity of the proposed sensor. The Raman intensity scales linearly with the negative logarithm of the CV concentration (−log C), yielding $R^2$ values of 0.948 and 0.951 for the 1177 $cm^{-1}$ and 1623 $cm^{-1}$ bands, respectively (Figure 6b,c). These results demonstrate that the FTW-SERS probe not only provides a low detection limit, but also enables reliable quantitative analysis over a broad dynamic range.

Reproducibility is a key requirement for practical SERS sensing. To evaluate fabrication consistency, three independent batches of probes were prepared under identical optimized conditions, and each probe was measured three times using $10^{-5}$ M CV. The corresponding intensity distributions at 1177 and 1623 $cm^{-1}$ are shown in Figure 6d,e. The relative standard deviations (RSDs) were calculated to be 4.32% and 4.68%, respectively, confirming excellent probe-to-probe reproducibility. Such low RSD values highlight the robustness of the laser-induced assembly strategy and the uniformity of the SERS-active interface formed on the FTW surface.

To quantitatively evaluate the SERS activity of the fabricated FTW-SERS substrate, the enhancement factor (EF) for CV was calculated according to [26].

$$EF = \frac{I_{SERS}}{I_{Raman}} \cdot \frac{C_{Raman}}{C_{SERS}} \quad (4)$$

where $I_{SERS}$ and $I_{Raman}$ represent the Raman intensities of CV at 1177 $cm^{-1}$ measured on the Ag NC-functionalized FTW and the bare FTW, respectively. As shown in Figure 6f,

for the characteristic peak located at 1177 $cm^{-1}$, the Raman signal intensity ($I_{Raman}$) of $10^{-2}$ M CV detected using the bare FTW was 909.60 a.u., whereas the SERS signal intensity ($I_{SERS}$) of $10^{-6}$ M CV obtained using the FTW-SERS probe of the same length reached 14,644.50 a.u. The concentrations $C_{SERS} = 10^{-6}$ M and $C_{Raman} = 10^{-2}$ M correspond to the analyte concentrations used for the SERS and normal Raman measurements, respectively. All measurements were performed under identical experimental conditions to ensure a valid comparison. Based on the characteristic band at 1177 $cm^{-1}$, the enhancement factor (EF) of the FTW-SERS substrate toward CV was calculated to be $1.61 \times 10^5$.

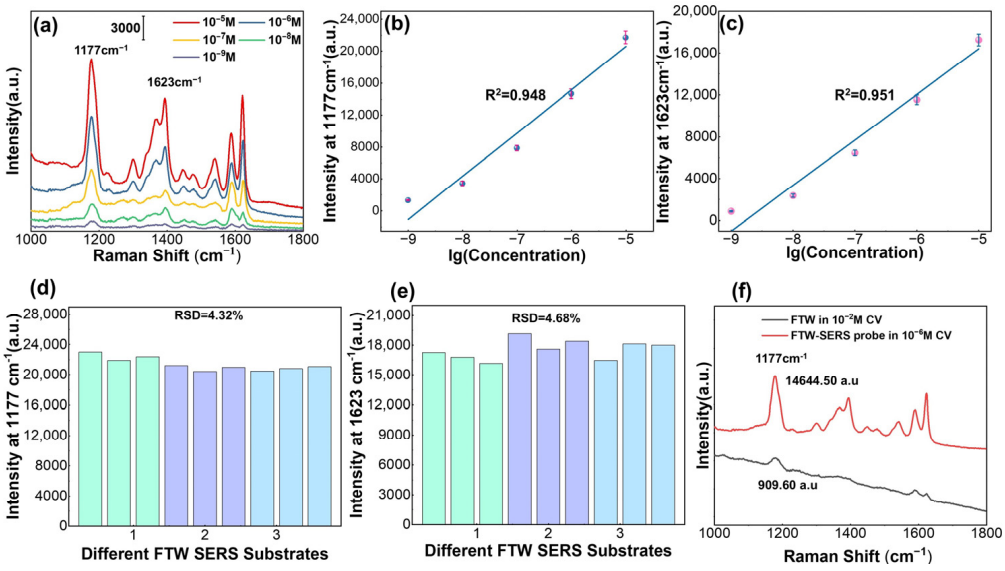



**Figure 6.** (**a**) SERS spectra of CV at different concentrations. Relationship between Raman intensity and concentration at 1177 $cm^{-1}$ (**b**) and 1623 $cm^{-1}$ (**c**). Raman intensities of $10^{-5}$ M CV at (**d**) 1177 $cm^{-1}$ and (**e**) 1623 $cm^{-1}$, obtained from three replicate measurements performed on three independent FTW SERS substrates. (**f**) The SERS signal of the FTW-SERS probe in the $10^{-6}$ M CV solution and the Raman signal of the bare FTW fiber in the $10^{-2}$ M CV solution.

### *3.3. Gas-Phase VOC Detection and Real-Time Breath Monitoring*

To evaluate practical applicability, acetone ($C_3H_6O$) and ethanol ($C_2H_5OH$) were selected as representative VOC targets. These molecules are not only relevant in industrial safety but also serve as important physiological biomarkers. Acetone is closely linked to lipid metabolism and diabetic conditions, whereas ethanol monitoring is widely used in clinical and forensic contexts.

Distinct Raman signatures are observed for both analytes, with characteristic peaks at 1452 $cm^{-1}$ for ethanol [27] and 790 $cm^{-1}$ for acetone [28]. As illustrated in Figure 7a,b, the sensor successfully resolved the characteristic spectral fingerprints of ethanol at 1452 $cm^{-1}$ (assigned to C-H asymmetric bending) and acetone at 790 $cm^{-1}$ (assigned to C-C symmetric stretching). Distinct Raman signals were discernible even at a low concentration of 50 ppm, confirming the high sensitivity and capability for quantitative trace-level VOC detection.

To further demonstrate its clinical utility, the sensor was applied to real-time breath analysis of a healthy volunteer after the consumption of 500 mL of beer (5% $v/v$ alcohol) under controlled temperature and humidity conditions. A background breath spectrum collected from the same volunteer prior to alcohol consumption was included for comparison. For each time point, measurements were performed in triplicate and the averaged spectrum was used for analysis to ensure reproducibility. As shown in Figure 7c, the ethanol Raman signal followed a characteristic pharmacokinetic trend, with a maximum observed at 30 min, corresponding to the absorption phase. The signal intensity then decreased to approximately 65% of the maximum at 60 min and to ~30% at 90 min, before becoming un-

detectable at 180 min, consistent with the elimination phase. The observed time-dependent spectral evolution agrees well with the known metabolic behavior of ethanol in the human body, demonstrating the potential of the proposed sensor for non-invasive, real-time monitoring of dynamic metabolic processes.

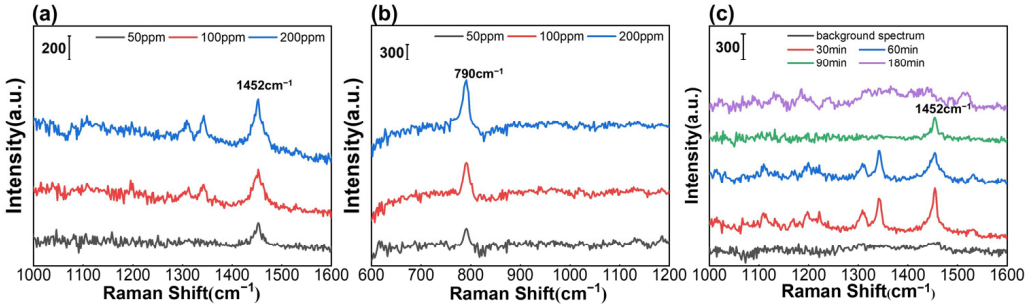



**Figure 7.** (**a**) SERS spectra of ethanol at different concentrations; (**b**) SERS spectra of acetone at different concentrations; (**c**) time-dependent SERS spectra of exhaled ethanol after alcohol consumption.

### *3.4. Performance Enhancement via Ag/GO Hybrid Interface and Humidity Regulation*

To further push the analytical limits of the sensor beyond the base sensor's capabilities, we integrated a graphene oxide (GO) functional layer (0.3 mg/mL, drop-casted) onto the Ag NC-FTW surface to construct an Ag/GO hybrid probe. This GO overlayer effectively enriches gas molecules at the sensing interface while preserving the strong localized electromagnetic enhancement provided by the underlying Ag NCs. Under identical measurement conditions (Figure 8), the GO modification lowered the minimum detectable concentration for both ethanol (monitored via the 1452 $cm^{-1}$ asymmetric CH3 bending mode) and acetone (788 $cm^{-1}$ symmetric C-C stretching mode) from 50 ppm to 25 ppm. This twofold sensitivity improvement is accompanied by a predictable, concentration-dependent attenuation in Raman peak intensities, confirming the hybrid probe's capability for reliable quantitative gas analysis.

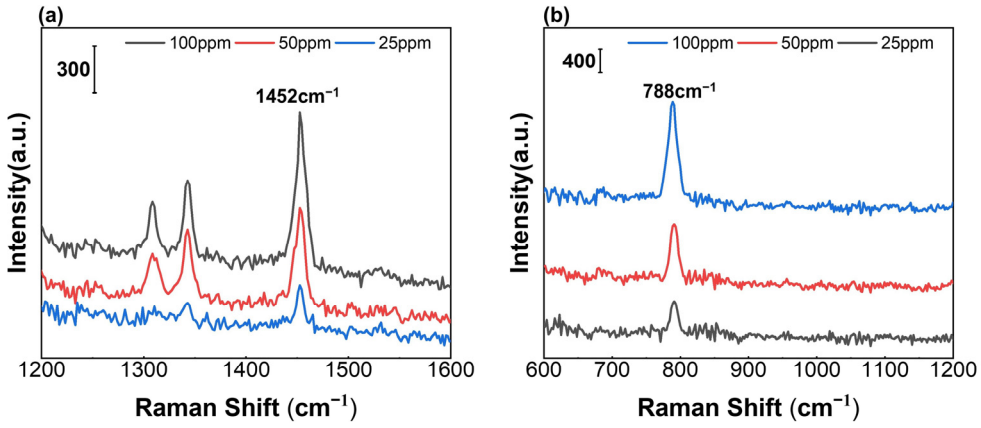



**Figure 8.** SERS spectra of (**a**) ethanol and (**b**) acetone at different concentrations obtained using the Ag/GO-functionalized FTW probe.

Clinical breath samples typically exhibit high relative humidity; however, their impact on Raman-based detection is intrinsically limited. Although water molecules may be present in excess, their interference with VOC sensing is mitigated through both system design and fundamental spectroscopic properties. At the system level, a pre-dehumidification channel is incorporated to suppress bulk water vapor condensation on the FTW surface, thereby stabilizing the measurement baseline. More importantly, water is an inherently weak Raman scatterer due to its low molecular polarizability, and its vibrational response

is dominated by broad O–H bands (~1640 $cm^{-1}$ and 3200–3600 $cm^{-1}$), which are spectrally well separated from the characteristic peaks of ethanol (1452 $cm^{-1}$) and acetone (788 $cm^{-1}$). As a result, even under fluctuating humidity conditions, residual water does not produce significant spectral overlap or background interference. This intrinsic spectral selectivity distinguishes Raman-based detection from infrared absorption techniques, where water typically introduces strong signal masking [29]. Therefore, the combination of spectral separation and system-level humidity regulation ensures stable and reliable sensing performance in complex breath environments, without requiring stringent humidity control.

Table 1 presents a comparative analysis of the proposed sensor with representative state-of-the-art gas detection technologies. Spectroscopic methods based on specialized optical fibers, as reported in Refs. [30,31], can achieve minimum detectable concentrations at the ppb level; however, these systems typically require complex optical alignment, high-cost light sources, and long gas exchange times, which limit their suitability for rapid and portable sensing. SERS-based approaches using planar substrates [32–34], while avoiding the complexity of hollow-core fiber configurations, often lack the flexibility, remote sensing capability, and in situ applicability of fiber-integrated probes, and may suffer from limited interaction volumes. In contrast, the proposed FTW-SERS sensor integrates the robustness of optical fibers with the strong plasmonic enhancement of Ag NCs under evanescent-wave excitation. Although the minimum detectable concentration (25 ppm) is higher than that of some laboratory-based techniques, the sensor provides a compact, alignment-free configuration and enables real-time detection, demonstrating its potential for practical breath analysis applications.

**Table 1.** Performance comparison of the proposed sensor with state-of-the-art gas sensors.

| Gas Species | Principle | Enhancement Material | Detectable Concentration | Ref. |
|---|---|---|---|---|
| $CO_2$ | LAS [1] | ~ | 5 ppm | [30] |
| CO, $CO_2$ | MIPS [2] | ~ | 35 ppb (CO); 120 ppb ($CO_2$) | [31] |
| $C_2H_6O$, $C_7H_8$, $C_3H_6O$, $H_2S$ | SERS | Au@$SnO_2$ | 500 ppm | [32] |
| $C_4H_8O$, $C_6H_{12}O$, $C_7H_6O$ | SERS | Ag@MOF | 3 ppb | [33] |
| $C_7H_8$, $C_8H_{10}$, $C_6H_5Cl$ | SERS | Au@MOF | Not mentioned | [34] |
| **$C_2H_6O$, $C_3H_6O$** | **SERS** | **Ag NCs + FTW** | **25 ppm (with GO)** | **This work** |

[1] LAS: Laser Absorption Spectroscopy; [2] MIPS: Mid-Infrared Photothermal Spectroscopy.

## 4. Conclusions

In summary, we demonstrate a highly sensitive and robust fiber-optic SERS gas sensing platform based on silver nanocubes assembled onto a fiber taper waist via an evanescent wave-assisted strategy. The extended evanescent field of the tapered structure increases the interaction volume and minimizes thermal damage compared to direct end-face illumination. This design yields a robust enhancement factor and high reproducibility (RSD < 5%). The sensor exhibits a broad dynamic range and high sensitivity, enabling the detection of aqueous crystal violet down to $10^{-9}$ M and gaseous ethanol and acetone at concentrations as low as 25 ppm when utilizing a GO-functionalized interface. Real-time breath tests on human subjects successfully tracked post-consumption ethanol metabolism, validating the sensor's clinical applicability. This alignment-free, integrated fiber-optic design offers a practical solution for continuous metabolic monitoring. Subsequent development will aim to improve sensor selectivity for complex gas mixtures to expand its diagnostic scope.

**Author Contributions:** Conceptualization, P.Z. and Z.Z.; methodology, W.W. and P.Z.; validation, W.W., T.W. and K.Z.; formal analysis, W.W., P.T. and Y.S.; investigation, W.W.; resources, P.Z.; data curation, W.W.; writing—original draft preparation, W.W.; writing—review and editing, P.Z. and Z.Z.;

visualization, W.W.; supervision, P.Z., J.Z. and Z.Z.; project administration, S.D. and P.Z.; funding acquisition, P.Z. and Z.Z. All authors have read and agreed to the published version of the manuscript.

**Funding:** This work was funded by the Natural Science Foundation of China (Nos. 62475124, 62075107), Zhejiang Provincial Natural Science Foundation of China (No. LR24F050001) and Key R&D Project of Ningbo City (No. 2023Z105).

**Data Availability Statement:** Data underlying the results presented in this paper are not publicly available at this time but may be obtained from the authors upon reasonable request.

**Conflicts of Interest:** The authors declare no conflicts of interest.

## References

1. Wang, Y.; Weng, H.; Xu, D.; Zhang, S. Comparison of Breath Biomarker Studies for Early Diagnosis of Chronic Kidney Disease: A Review. *J. Breath Res.* **2025**, *19*, 034002. [CrossRef]
2. Sun, S.; Li, X.; Wang, N.; Huang, B.; Li, X. A Sensitive Ppb-Level $NO_2$ Sensor Based on $SnO_2$ Decorated Te Nanotubes. *Sens. Actuators B Chem.* **2025**, *428*, 137238. [CrossRef]
3. Song, Y.; Yang, M.; Luo, X.; Zhang, X.; Zhou, S. Measurement of Exhaled Ammonia Based on Mid-Infrared EC-QCL and Flexible Hollow Waveguide: A New Idea for Early Diagnosis of Nephropathy. *IEEE Trans. Instrum. Meas.* **2025**, *74*, 9521807. [CrossRef]
4. Dong, H.; Li, X.; Liu, Y.; Cheng, W.; Han, C.; Yin, Y.; Li, X.; Shao, C.; Liu, Y. Wearable, Breathable, and Wireless Gas Sensor Enables Highly Selective Exhaled Ammonia Detection and Real-Time Noninvasive Illness Diagnosis. *ACS Sens.* **2025**, *10*, 3964–3975. [CrossRef] [PubMed]
5. Liu, X.; You, X.; Cui, X.; Fu, H.; Song, F.; Zhang, K.; Tang, Z.; Yu, S.; Yang, C.; Li, Q.; et al. A High-Performance Room-Temperature Biomass Carbon-Based Nitric Oxide (NO) Gas Sensor Used to Diagnose Asthma and Monitor Its Severity Clinically. *Microchem. J.* **2025**, *215*, 114019. [CrossRef]
6. Dai, J.; Ye, T.; Zhan, X.; Han, S.; Ma, B.; Hai, H.; Liu, Y.; Tao, P.; Li, D.; Wang, F.; et al. A Room-Temperature Dual-Gas Humidity/Ammonia Sensor Based on Gallium Oxide for Breath Analysis. *IEEE Sens. J.* **2025**, *25*, 9384–9392. [CrossRef]
7. Yu, Y.; Cao, X.; Li, C.; Zhou, M.; Liu, T.; Liu, J.; Zhang, L. A Review of Machine Learning-Assisted Gas Sensor Arrays in Medical Diagnosis. *Biosensors* **2025**, *15*, 548. [CrossRef] [PubMed]
8. Wu, H.; Zeng, R.; Li, L.; Li, M.; Zhu, Y.; Li, W.; Zhao, B.; Wen, C.; Feng, F. Exhaled Gas Biomarkers: A Non-Invasive Approach for Distinguishing Diabetes and Its Complications. *Analyst* **2025**, *150*, 3636–3642. [CrossRef]
9. Van Den Berg, S.; Zaat, A.S.; Van Der Poel, I.F.; Van Dijk, Y.E.; Hashimoto, S.; Rutjes, N.W.P.; Terheggen-Largo, S.W.J.; Van Ewijk, B.E.; Gagliani, C.; Sondaal, F.L.; et al. Uncovering Non-Invasive Biomarkers in Paediatric Severe Acute Asthma Using Targeted Exhaled Breath Analysis. *Metabolites* **2025**, *15*, 247. [CrossRef] [PubMed]
10. Tang, Z.; Yang, J.; Su, B.; Xu, X.; Luo, X.; Wang, H.; Zhang, K.; Huan, T.; Sinues, P.; Fang, M.; et al. Metabolite Fusion between Breath and Blood Enables More In-Depth Understanding of the Endogenous Metabolome. *Anal. Chem.* **2025**, *97*, 19427–19436. [CrossRef]
11. Woollam, M.; Christensen, A.; Schulz, E.; Eckerle, S.; Davis, M.D.; Sanders, D.B.; Agarwal, M. Systematic Comparison of Methods for Offline Breath Sampling. *Anal. Bioanal. Chem.* **2025**, *417*, 5061–5076. [CrossRef] [PubMed]
12. Huo, Y.; Zhao, J.; Wang, T.; Wang, T.; Yu, H.; Dong, X.; Yang, Y. RGO Induced Oxygen Vacancy at the $SnO_2$ Contact Surface as ppb Level Flexible Low Temperature $NO_2$ Gas Sensor. *Microchem. J.* **2025**, *216*, 114755. [CrossRef]
13. Dwyer, D.B.; Niedziela, J.L.; Miskowiec, A. Tandem Pyrolysis Evolved Gas–Gas Chromatography–Mass Spectrometry. *J. Anal. Appl. Pyrolysis* **2025**, *186*, 106904. [CrossRef]
14. Glöckler, J.; Mitrovics, J.; Beeken, S.; Leja, M.; Welearegay, T.; Österlund, L.; Haick, H.; Shani, G.; Di Natale, C.; Murillo, R.; et al. Infrared Spectroscopic Electronic Noses: An Innovative Approach for Exhaled Breath Sensing. *ACS Sens.* **2025**, *10*, 427–438. [CrossRef] [PubMed]
15. Xu, D.; Liu, P.; Meng, X.; Chen, Y.; Du, L.; Zhang, Y.; Qiao, L.; Zhang, W.; Kuang, J.; Liu, J. Design of an Electronic Nose System with Automatic End-Tidal Breath Gas Collection for Enhanced Breath Detection Performance. *Micromachines* **2025**, *16*, 463. [CrossRef]
16. Rescalli, A.; Vegetali, G.; Gelosa, S.; Cellesi, F.; Cerveri, P. AI-Based Quantification of Volatile Organic Compounds in Gas Mixtures Exploiting Temperature Modulation of MOS Sensor Array. *IEEE Sens. J.* **2025**, *25*, 26324–26337. [CrossRef]
17. Khetani, A.; Momenpour, A.; Alarcon, E.I.; Anis, H. Hollow Core Photonic Crystal Fiber for Monitoring Leukemia Cells Using Surface Enhanced Raman Scattering (SERS). *Biomed. Opt. Express* **2015**, *6*, 4599. [CrossRef]
18. Merdalimova, A.A.; Rudakovskaya, P.G.; Ermatov, T.I.; Smirnov, A.S.; Kosolobov, S.S.; Skibina, J.S.; Demina, P.A.; Khlebtsov, B.N.; Yashchenok, A.M.; Gorin, D.A. SERS Platform Based on Hollow-Core Microstructured Optical Fiber: Technology of UV-Mediated Gold Nanoparticle Growth. *Biosensors* **2021**, *12*, 19. [CrossRef]

19. Qiu, H.W.; Xu, S.C.; Jiang, S.Z.; Li, Z.; Chen, P.X.; Gao, S.S.; Zhang, C.; Feng, D.J. A Novel Graphene-Based Tapered Optical Fiber Sensor for Glucose Detection. *Appl. Surf. Sci.* **2015**, *329*, 390–395. [CrossRef]
20. Al-Qazwini, Y.; Noor, A.S.M.; Yaacob, M.H.; Harun, S.W.; Mahdi, M.A. Experimental Realization and Performance Evaluation of Refractive Index SPR Sensor Based on Unmasked Short Tapered Multimode-Fiber Operating in Aqueous Environments. *Sens. Actuators A Phys.* **2015**, *236*, 38–43. [CrossRef]
21. Wang, L.; Sun, Y.; Li, Z. Dependence of Raman Intensity on the Surface Coverage of Silver Nanocubes in SERS Active Monolayers. *Appl. Surf. Sci.* **2015**, *325*, 242–250. [CrossRef]
22. Pahurkar, V.G.; Tamgadge, Y.S.; Gambhire, A.B.; Muley, G.G. Evanescent Wave Absorption Based Polyaniline Cladding Modified Fiber Optic Intrinsic Biosensor for Glucose Sensing Application. *Measurement* **2015**, *61*, 9–15. [CrossRef]
23. Horita, Y.; Ishimi, M.; Negishi, Y. Anion-Templated Silver Nanoclusters: Precise Synthesis and Geometric Structure. *Sci. Technol. Adv. Mater.* **2023**, *24*, 2203832. [CrossRef]
24. Jiang, T.; Wang, B.; Zhang, L.; Zhou, J. Hydrothermal Synthesis of Silver Nanocubes with Tunable Edge Lengths and Their Size Dependent SERS Behaviors. *J. Alloys Compd.* **2015**, *632*, 140–146. [CrossRef]
25. Zhang, F.; Huang, Q.; Li, X.; Yang, S.; Li, D.; Lu, W.; Zhao, S.; Gao, Y.; Yang, J. Multi-Responsive Hydrogels with Dual-Dynamic Covalent and Hydrogen-Bonded Networks: Aldehyde-Functionalised Silica Reinforced β-Cyclodextrin/Hyaluronic Acid Frameworks for Enhanced Breast Cancer Therapy and Inflammation Suppression. *J. Colloid Interface Sci.* **2026**, *706*, 139497. [CrossRef] [PubMed]
26. Yin, Y.; Wang, M.; Xu, T.; Yin, C.; Jin, Y. SERS Chip Fabricated by the Thermal Effect in a Double-Metal-Cladding Waveguide. *Appl. Opt.* **2020**, *59*, 11070. [CrossRef] [PubMed]
27. Dai, S.-M.; Shen, Y.; Wang, J.-X.; Zhang, X.-X.; Zhang, Y.-Y.; Huang, Y.-Y.; Su, R.-H.; Yan, J. Identification of Green Tea Varieties and Origins Based on Fused Surface Enhanced Raman Spectra from Different Extraction Solvent. *Spectrochim. Acta Part A Mol. Biomol. Spectrosc.* **2026**, *348*, 127220. [CrossRef]
28. Zhang, X.; Lei, Y.; Song, R.; Chen, W.; Wang, C.; Wang, Z.; Yin, Z.; Wan, F. Quantitative Analysis of Acetone in Transformer Oil Based on ZnO NPs@Ag NWs SERS Substrates Combined with a Stoichiometric Model. *Int. J. Mol. Sci.* **2022**, *23*, 13633. [CrossRef]
29. Sommers, G.M.; Calegari Andrade, M.F.; Zhang, L.; Wang, H.; Car, R. Raman Spectrum and Polarizability of Liquid Water from Deep Neural Networks. *Phys. Chem. Chem. Phys.* **2020**, *22*, 10592–10602. [CrossRef]
30. Nikodem, M.; Gomółka, G.; Klimczak, M.; Pysz, D.; Buczyński, R. Laser Absorption Spectroscopy at 2 μm inside Revolver-Type Anti-Resonant Hollow Core Fiber. *Opt. Express* **2019**, *27*, 14998. [CrossRef]
31. Zheng, K.; Bao, H.; Luo, W.; Liu, F.; Chen, F.; Liao, H.; Zhao, S.; Jiang, S.; Zheng, C.; Ho, H.L.; et al. Hollow-Core Fiber-Based Mid-Infrared Photothermal Spectroscopy for Multi-Component Gas Sensing. *IEEE J. Sel. Top. Quantum Electron.* **2024**, *30*, 5600606. [CrossRef]
32. Bao, H.; Motobayashi, K.; Zhang, H.; Cai, W.; Ikeda, K. In-Situ Surface-Enhanced Raman Spectroscopy Reveals a Mars–van Krevelen-Type Gas Sensing Mechanism in Au@$SnO_2$ Nanoparticle-Based Chemiresistors. *J. Phys. Chem. Lett.* **2023**, *14*, 4113–4118. [CrossRef] [PubMed]
33. Huang, L.; Zhu, Y.; Xu, C.; Cai, Y.; Yi, Y.; Li, K.; Ren, X.; Jiang, D.; Ge, Y.; Liu, X.; et al. Noninvasive Diagnosis of Gastric Cancer Based on Breath Analysis with a Tubular Surface-Enhanced Raman Scattering Sensor. *ACS Sens.* **2022**, *7*, 1439–1450. [CrossRef] [PubMed]
34. Chen, Q.-Q.; Hou, R.-N.; Zhu, Y.-Z.; Wang, X.-T.; Zhang, H.; Zhang, Y.-J.; Zhang, L.; Tian, Z.-Q.; Li, J.-F. Au@ZIF-8 Core–Shell Nanoparticles as a SERS Substrate for Volatile Organic Compound Gas Detection. *Anal. Chem.* **2021**, *93*, 7188–7195. [CrossRef] [PubMed]


**Disclaimer/Publisher's Note:** The statements, opinions and data contained in all publications are solely those of the individual author(s) and contributor(s) and not of MDPI and/or the editor(s). MDPI and/or the editor(s) disclaim responsibility for any injury to people or property resulting from any ideas, methods, instructions or products referred to in the content.